Optically Enabled ADCs and Application to Optical Communications

ANDREA ZAZZI[1], **JULIANA MÜLLER**[1], **MAXIM WEIZEL**[2], **JONAS KOCH**[3], **DENGYANG FANG**[4],
ALVARO MOSCOSO-MÁRTIR[1], **ALI TABATABAEI MASHAYEKH**[1], **ARKA D. DAS**[1], **DANIEL DRAYß**[4],
FLORIAN MERGET[1], **FRANZ X. KÄRTNER**[5,6] (Fellow, IEEE),
STEPHAN PACHNICKE[3] (Senior Member, IEEE), **CHRISTIAN KOOS**[4],
J. CHRISTOPH SCHEYTT[2], **AND JEREMY WITZENS**[1] (Senior Member, IEEE)

(Invited Paper)

[1]Institute of Integrated Photonics, RWTH Aachen University, 52074 Aachen, Germany

[2]Heinz Nixdorf Institute, University of Paderborn, 33102 Paderborn, Germany

[3]Chair of Communications, Kiel University, 24143 Kiel, Germany

[4]Institute of Photonics and Quantum Electronics, Karlsruhe Institute of Technology, 76131 Karlsruhe, Germany

[5]Department of Ultrafast Optics and X-Rays, German Electron-Synchrotron (DESY), 22607 Hamburg, Germany

[6] Department of Physics, University of Hamburg, 22607 Hamburg, Germany

CORRESPONDING AUTHOR: J. WITZENS (e-mail: jwitzens@iph.rwth-aachen.de)

This work was supported in part by the German Research Foundation in the framework of the priority program "Electronic-Photonic
Integrated Systems for Ultrafast Signal Processing," projects "Ultra-Wideband Photonically Assisted Analog-to-Digital Converters"
and "Nonlinear Fourier Transform-based Optical Transmission using Electronic-Photonic Signal Processing."

(Andrea Zazzi and Juliana Müller contributed equally to this work.)

ABSTRACT Electrical-optical signal processing has been shown to be a promising path to overcome the limitations of state-of-the-art all-electrical data converters. In addition to ultra-broadband signal processing, it allows leveraging ultra-low jitter mode-locked lasers and thus increasing the aperture jitter limited effective number of bits at high analog signal frequencies. In this paper, we review our recent progress towards optically enabled time- and frequency-interleaved analog-to-digital converters, as well as their monolithic integration in electronic-photonic integrated circuits. For signal frequencies up to 65 GHz, an optoelectronic track-and-hold amplifier based on the source-emitter-follower architecture is shown as a power efficient approach in optically enabled BiCMOS technology. At higher signal frequencies, integrated photonic filters enable signal slicing in the frequency domain and further scaling of the conversion bandwidth, with the reconstruction of a 140 GHz optical signal being shown. We further show how such optically enabled data converter architectures can be applied to a nonlinear Fourier transform based integrated transceiver in particular and discuss their applicability to broadband optical links in general.

INDEX TERMS Photonic integrated circuits, silicon photonics, analog-to-digital conversion, signal sampling, time-interleaved ADCs, spectrally-sliced ADCs, optically enabled ADCs, optical fiber communication, nonlinear distortion, nonlinear Fourier transform, solitons.

I. INTRODUCTION

WITH the large scale deployment of coherent optical fiber links towards the end of the first decade of the 21st century, the availability and performance of high-speed data converters has first become a bottleneck and later a key performance driver for long-haul communications [1]. Since then, the use of digital signal processing (DSP) has become pervasive in optical transceiver technologies and has even penetrated high-end direct detection such as 400G data center transceivers [2] as well as direct detection 5G backhaul interconnects [3].

In order to meet ever growing performance requirements, a number of architectures have been explored to increase analog-to-digital converter (ADC) bandwidth and sampling

rates, while maintaining a sufficient effective number of bits (ENOB) [4]. A common technique applied in high-speed communications is time interleaving, that consists in interleaving several ADCs, each clocked at a subdivided sampling rate and with an offset clock phase, in order to digitize a faster signal [5], [6]. Frequency interleaving is another such technique [7], in which a broadband signal is sliced into several tributaries each covering a reduced passband. These are then down-converted and digitized with reduced sampling rates. The resulting digital signals are finally stitched back together to recover the broadband signal. While spectral slicing has been used in high-end oscilloscopes [8], it appears to be less common in more cost sensitive applications such as optical transceivers. Nonetheless, efforts are being made to adapt it to the requirements of optical communications, for example by implementing backpropagation based signal equalization that does not require interruption of service for training [9].

Light has proven to be the vehicle of choice to transport broadband information over extended distances, and, with data rates continuously rising, optical communications is being applied to ever shorter distances [10], currently down to a few meters. It has also proven to have superior properties for the processing of broadband waveforms in microwave photonics [11]. In this context, it has shown its potential for further extending the limits of ADC performance [12], in particular by implementing the high-speed front-end of time-interleaved [13] or spectrally-sliced [14] ADCs. Besides their potential for extending the analog bandwidth of ADCs beyond the range of pure electronics, the ultra-low jitter associated to the pulse train of certain mode-locked lasers (MLLs), down to the attosecond range [15], can be leveraged to considerably increase the aperture jitter limited ENOB of optically enabled ADCs [13].

However, while optically enabled ADCs built out of discrete components have shown impressive performance, the performance of integrated systems has so for lagged significantly behind [13]. Constant improvement in electronic-photonic integration is however paving the way for integrating such systems at the chip scale. Silicon photonics (SiP) in particular offer a platform for scalable integration and, in some cases, even monolithic co-integration of electronics and photonics [16].

In this paper, we review some of our recent work on chip-scale integrated time-interleaved and spectrally-sliced photonically enabled ADCs, with a particular focus on the integration of optical filters with electronic receiver and sampling circuits in electronic-photonic integrated circuits (ePICs). Work on in-package integration of ultra-broadband modulators [17], [18] by means of multi-chip assemblies as well as miniaturization of low jitter comb sources is also under way, but not covered here in details. After covering time-interleaved and spectrally-sliced ADCs in Sections II and III, as well as a use case of frequency stitching in broadband coherent receivers utilizing the nonlinear Fourier transform (NFT) in Section IV, we give an outlook on optically enabled ADCs in optical communications in Section V.

II. TIME-INTERLEAVED ADCS

Different techniques have been proposed to implement time-interleaved photonic samplers, most of which rely on ultra-low-jitter MLLs as a clock reference [12]. A widely investigated approach is to use an electro-optic modulator (EOM), such as a Mach-Zehnder modulator (MZM), to modulate an electrical input signal onto the intensity of an MLL pulse train [13]. Applying different delays to spectral slices of the MLL spectrum, interleaved pulse trains with different center frequencies are first created. After modulation, the pulses are separated by frequency and sent to multiple photodetectors, subdividing the required electrical bandwidth.

Alternatively, the MLL pulse train can first be converted into the electrical domain to supply a low jitter clock signal to an electrical circuit [19], [20]. Both techniques allow leveraging the low jitter afforded by certain classes of MLLs [15], as opposed to combs generated by electro-optic transduction of radio-frequency (RF) pulse trains [21] that are subject to the jitter of the electric source.

In previous work by Krueger *et al.*, in direct analogy to the operation implemented by the MZM in the electro-optic domain, that is, multiplying the electrical signal with the optical pulse trains, the electrical signal has been multiplied with a transduced optical pulse train by means of a mixer, the output of which was further routed to interleaved integrating electrical ADCs [19]. Here, we use the transduced optical pulse train as an electrical clock to control a switched-emitter-follower (SEF) track-and-hold amplifier (THA) with a high bandwidth exceeding 65 GHz for broadband analog-to-digital signal conversion. The opto-electronic (OE) circuit and its performance are described in this section. The interested reader will find a more detailed circuit analysis in [20].

A. OE-SEF THA ARCHITECTURE

Fig. 1(a) shows a micrograph of the OE-SEF chip, which covers an area of 0.59 mm^2 and is fabricated in the silicon photonic 250 nm SiGe BiCMOS technology ($f_T = 220$ GHz) of the Leibniz Institute for Innovative Microelectronics (IHP), that allows for monolithic integration of photonic and electronic components [22]. The chip has a symmetric layout given the differential nature of the circuit. In this architecture, a grating coupler (GC) is used to couple the optical pulse train generated by an MLL into the chip, in which an electrical clock signal is generated through an integrated waveguide photodiode (PD) followed by a transimpedance amplifier (TIA). A simplified schematic of the common-base (Q_1) TIA, with a transimpedance of $R_1 = 100$ Ω, followed by an emitter-follower buffer (Q_3) is shown in Fig. 2. When no light arrives at the photodiode, the TIA is biased to guarantee a higher voltage at node H than at node T and the SEF sampler circuit (not shown) operates in hold mode. On the other hand, when light is received by the photodetector, the voltage at node H is pulled down and the SEF switches to track mode. The voltage at node T is controlled through external biasing leading to a pseudodifferential clock signal.
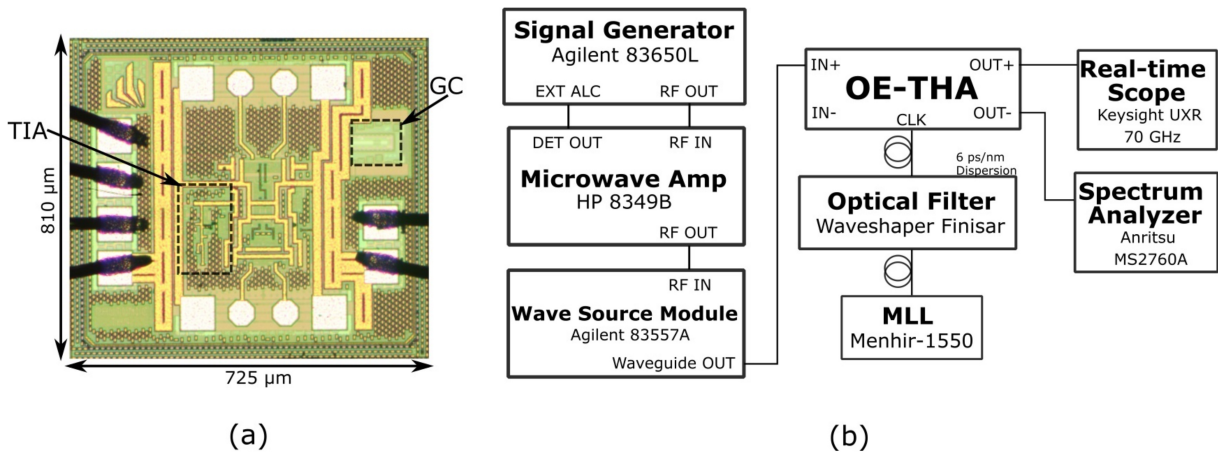
FIGURE 1. (a) Micrograph of the chip implementing the OE-THA. Dashed insets show the grating coupler and the transimpedance amplifier. (b) Dynamic measurement setup for input frequencies above 50 GHz. From 0-50 GHz, the signal generator output is directly connected to the THA input.

The first TIA stage was implemented using a common base stage to leverage its low input impedance and thus potential for high bandwidth, its low power consumption, and stable PD biasing, which varies very little with the applied optical power and is controlled by the externally applied voltage V_{pd_bias}. These are important characteristics here as a sampling rate of 30 GS/s was initially targeted, with measurement results reported in the following limited by the repetition rate of the MLL, and the optical pulses undergo a large dynamic range. It also proved adequate from the perspective of noise performance, that is less of an issue here than in a typical communications setting. Indeed, as discussed in the following, the MLL emits pulses with a very high peak power over 100 W, so that the excess noise of the TIA leads to very little excess clock jitter. Instead, saturation of PD and TIA is an aspect that needs further investigation, as explained in the following.

A single-ended common-base TIA architecture was chosen in this first iteration due to its small footprint, simplicity and proven suitability as shown in [22]. The architecture can actually be considered pseudo-differential, since the single-ended output of the TIA is converted to a differential signal by the SEF stage. The TIA's second input, V_{ext_bias}, is set by an external voltage source to maintain controllability during experiments. Its optimum value depends not only on the average optical power, but also on the TIA bandwidth and the time-domain pulse shape. Mismatch resulting from fabrication tolerances can be overcome by this external controllability. While a high linearity does not play a role in this TIA aimed at trigger-signal generation, fully differential architectures present advantages in terms of signal-to-noise ratio (SNR) and supply noise rejection [23], [24] and will be considered in future chip iterations.

The circuit can in principle be operated in the −40°C to 125°C temperature range specified for the chosen technology. Characterization was done at 27°C. Simulations show an accumulated input referred root-mean-square (rms) noise current of 3.85 µA at 27°C which rises almost linearly to
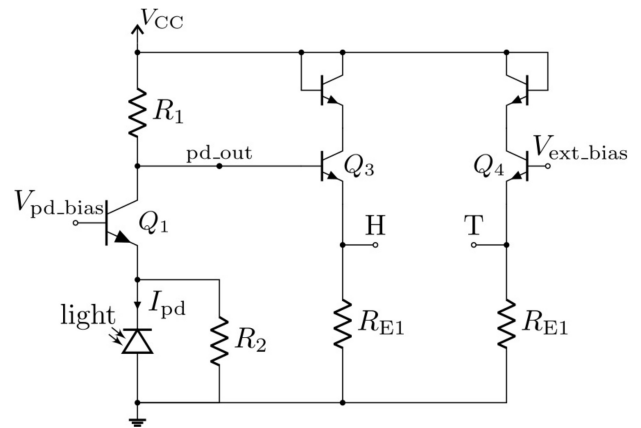

FIGURE 2. Simplified schematic of the common-base transimpedance amplifier used to convert the optical pulse train into a pseudo-differential electrical clock signal.

4.3 µA at 125°C (integrated up to 35 GHz). The simulated gain and bandwidth drop from 42.5 dB to 42 dB and from 31.5 GHz to 28.5 GHz, respectively.

The SEF architecture has been chosen for the THA due to its performance in terms of bandwidth and resolution, which have been shown to be superior to other electronic sampler architectures in bipolar technologies.

B. MEASUREMENT SETUP AND EXPERIMENTAL RESULTS

The measurements presented in the following were performed in a single-ended configuration. The S-parameters of the THA were measured with a vector network analyzer (Anritsu VNA MS4647b), with de-embedded cables and high frequency (HF) ground-signal-signal-ground (GSSG) probes, revealing a track-mode small-signal 3-dB bandwidth of 65 GHz. Hold-mode feedthrough was measured to stay below −30 dB up to 40 GHz, rise to −21 dB at 50 GHz, and drop again for higher frequencies. In these measurements, the circuit was sequentially set to track- or hold-mode through external bias, circumventing the PD and TIA subsystem.
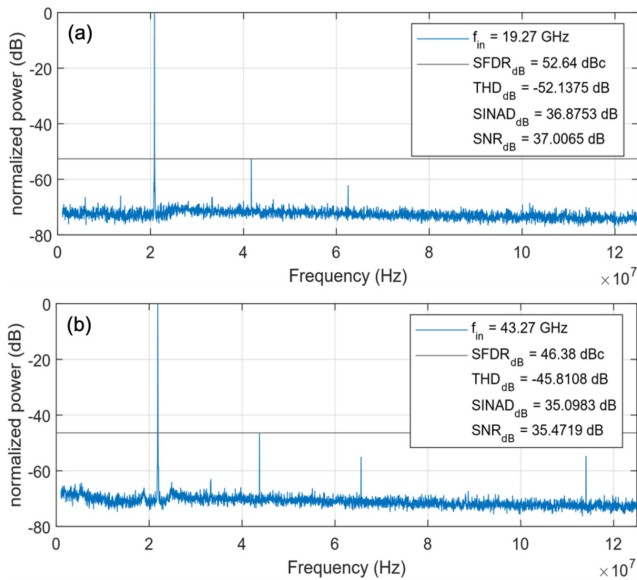
FIGURE 3. Normalized spectra and extracted figures of merit for electrical input signal power $P_{in} = -10$ dBm and (a) input frequency $f_{in} = 19.27$ GHz, (b) $f_{in} = 43.27$ GHz. Resolution and video bandwidth are set to 1 kHz.

To evaluate the switched, dynamic performance, the measurement setup shown in Fig. 1(b) is used. The signal-generator output is directly connected to the chip via an HF-probe for frequencies below 50 GHz. Above, the signal is first amplified by a microwave amplifier (HP 8349B) and then quadrupled by a millimeter-wave source module (Agilent 83557A). The optical sampling clock is generated by a solid-state MLL (MENHIR-1550) with a free spectral range (FSR) of 250 MHz and a temporal full width at half maximum (FWHM) of 250 fs. A tunable optical processor further introduces a predefined dispersion of 6 ps/nm prior to coupling the light into the chip through a GC, resulting in a pulse FWHM of 60 ps after dispersion assuming the laser to emit Fourier transform limited hyperbolic secant pulses as per its data sheet.

Transient responses are reported in [20]. Here, we show measurements recorded by connecting the electrical output to a spectrum analyzer set to a 1 kHz resolution bandwidth (RBW). Two exemplary spectra are shown in Fig. 3. These are further analyzed to assess multiple figures of merit, among which the signal-to-noise and distortion ratio (SINAD or SNDR), the total harmonic distortion (THD), the spurious free dynamic range (SFDR) and the SNR.

Fig. 4 reports the achieved SINAD and the corresponding ENOB as a function of the input signal frequency for varying input powers. The circuit presents an ENOB larger than 5.5 bits SINAD up to approximately 45 GHz and, depending on the input power, over 5 bits SINAD up to 65 GHz. The equivalent jitter ranges from 55 fs to 80 fs up to frequencies in excess of 65 GHz. The best equivalent jitter is achieved at 41 GHz with 55.8 fs rms at −5 dBm electrical input power.

C. DISCUSSION ON PULSE-SHAPING
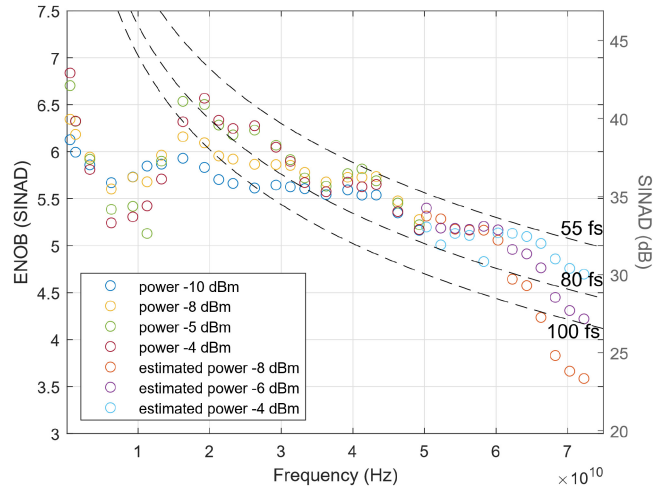Since the dynamic response of the OE-THA is assessed with a 250 MHz pulse repetition rate that is much below

FIGURE 4. ENOB (SINAD) as a function of frequency for varying electrical input signal powers. Dashed lines show the 55 fs, 80 fs and 100 fs equivalent jitter limits.

the 130 GS/s required to directly measure a 65 GHz signal, the resulting digitized signal is down-converted to below the corresponding 125 MHz Nyquist frequency. Nonetheless, the resulting signal strength enables verification of the adequateness of the OE-THA for the conversion of fast signals. In particular, the good ENOB obtained over the entire measurement range up to 70 GHz shows that the OE-THA switches from track- to hold-mode in a sufficiently short time to digitize fast signals. The full potential of the OE-THA can then be reached by increasing the MLL repetition rate, and, if this reaches an upper limit, by interleaving several OE-THAs with clock signals provided by interleaved pulse trains generated from a same reference laser by differential time delays [25]. The question then remains what pulse train repetition rates can be supported by this OE circuit.

Dynamic measurement results vary significantly depending on the dispersion externally applied to the pulse train. With settings ranging from 1 ps/nm to 10 ps/nm, 6 ps/nm has been empirically determined to be the optimum. Based on simulations, the dispersion induced by the GC and on-chip waveguides is too small to play a role here, so that the additional dispersion induced by the optical processor does not serve as dispersion compensation. Rather, it directly broadens the pulse in the time domain to ∼60 ps and reduces the peak power accordingly. Broader pulses require less bandwidth from the detection electronics and allow the SEF sufficient time for tracking. However, it is also possible that the corresponding reduction of peak power in the 100 mW range (on chip) was instrumental in reducing two-photon absorption in silicon waveguides and preventing saturation effects in germanium PDs or in the following circuitry. Indeed, OE switching of the OE-THA was experimentally observed up to an 18 GHz switching rate utilizing a continuous wave laser modulated with a sine wave by an external MZM, as limited by the cutoff frequency of the modulator [20]. Simulations indicate that switching should be supported up to 30 GHz with the current circuit, so that 4 interleaved stages

should be able to reach close to the 130 GS/s sampling rate required to make full use of the analog bandwidth. Efforts are also under way to increase this to a 60 GHz switching speed to reduce the required number of interleaved stages and to better understand the input power limitations of the PD+TIA. Interleaving two stages switched at 60 GHz would lead to a power efficient architecture for 120 GS/s sampling, as the signal path already supports a 65 GHz analog bandwidth and upgrading the switching speed of the clock path would only require very little extra power. Using a larger number of interleaved channels would otherwise waste the available 65 GHz analog bandwidth and associated power consumption.

Indeed, increasing the switching speed would result in a very small power consumption increase in the signal path, since it is designed in a "current mode logic" architecture with a constant current that is only switched between paths depending on the input signal and clock. Its static power consumption is 440 mW and only marginally rises as the sampling frequency is increased (simulations indicate less than 1 mW as the sampling speed is increased from 1 GS/s to 20 GS/s).

Most of the clock path is also designed as a current mode architecture. In the common-base TIA, an increase in photocurrent reduces V_{pd_out} and thus the current through Q_3, also stabilizing power consumption by offsetting the drawn current. As the sampling rate increases from 1 GS/s to 20 GS/s, the simulated power consumption of the clock path only increases from 75 mW to 78 mW.

The short pulse duration afforded by optical pulse generation facilitates the increase in sampling rate targeted here and fast rise-times increase the tolerance to noise in the clock path, suppressing its conversion to clock jitter. However, realizing low jitter optical pulse trains in compact devices and integrating them with the electronics developed here comes with challenges. One approach that is currently being investigated is to integrate rare-earth MLLs on chip [26]. Alternatively, the parametric generation of combs with high-quality-factor silicon nitride microrings is readily amenable to compact integration in multi-chip assemblies [27]–[29]. Both approaches can be combined with the remaining opto-electronics with photonic wire bonds [30].

D. OUTLOOK ON TI-ADCS AND OE-THA
The presented circuit exhibits a small-signal bandwidth in excess of 65 GHz and an ENOB larger than 5 bits SINAD over this entire signal range. The corresponding equivalent jitter for frequencies above 20 GHz ranges from 55 fs to 80 fs, resulting in a record resolution, once transferred to a complete ADC system [31].

Table 1 summarizes a comparison with the state of the art. In [19], the same ePIC technology has been adopted and, although the circuit was tested with higher sampling rates, the OE-SEF-THA analyzed here provides a comparable THD over a larger frequency range with a substantially lower power consumption. In addition, the OE-THA achieves

TABLE 1. Optically enabled samplers: comparison to state of the art.

	[19]	[13]	[13]	THIS WORK
Topology	Optically clocked	MZM sampler	MZM sampler	Optically clocked
Sampl. Rate	10 GS/s	2.1 GS/s	2.1 GS/s	0.25 GS/s
BW	30 GHz	41 GHz	-	65 GHz
THD/SFDR @f_{in}	-39 dB/42 dBc @32.5 GHz	-/52 dBc @41 GHz	-/39 dBc @10 GHz	-38 dB/39 dBc @43 GHz
ENOB @f_{in}	5.57 (SNR) @10 GHz	7 (SINAD) @41 GHz	3.5 (SINAD) @10 GHz	5.5 (SINAD) @45 GHz
Power	1250 mW	-	-	506 mW
Die Area	4.84 mm^2	-	-	0.59 mm^2
Process	250 nm photonic SiGe BiCMOS	Discrete components	Integrated silicon photonics	250 nm photonic SiGe BiCMOS

the highest bandwidth and ENOB among the surveyed integrated solutions for input frequencies over 10 GHz. As by Table 1, MZM-based discrete photonic samplers have shown remarkable results, although their chip-scale integrated counterparts have shown significantly lower performance [13]. MZM-based sampling requires DSP to compensate for the cosine-shaped transfer characteristic of the utilized MZM [13], in contrast to the high linearity of the SEF-THA used here. Furthermore, achieving bandwidths above 40 GHz with all-silicon depletion type MZMs as available in open-access ePIC technologies becomes increasingly difficult without stark degradation of other performance metrics such as required drive voltage and insertion losses [32], making the OE-SEF-THA with its 65 GHz bandwidth, excellent linearity, and no additional DSP requirements competitive in comparison [33].

III. SPECTRALLY-SLICED ADCS
Spectral slicing of the input signal is an alternative approach to time interleaving that has been applied to high-speed data conversion, both in all-electrical and optically enabled ADCs. The optically enabled, spectrally-sliced ADC presented in this section is based on the combination of an ultra-broadband EOM [17], [18], employed to convert the RF input signal into the optical domain, and an ePIC implementing spectral slicing and coherent detection of the aforementioned modulated signal. Electronic-photonic integration combines high scalability and low cost and enables scaling of spectrally sliced data converters to achieve large analog bandwidths with high ENOB.

Fig. 5(a) shows the architecture of the spectrally-sliced ADC. The modulated optical signal is spectrally sliced in the ePIC with integrated optical passband filters whose bandwidth matches that of the co-integrated PDs and electronic TIAs. Reduced speed electronic conversion is enabled by down-conversion of the optical signals, obtained through optical mixing of individual spectral slices with MLL lines serving as local oscillators (LO) and subsequent photodetection. MLLs generate tones on a regular spectral grid determined by their FSR, that can be selected
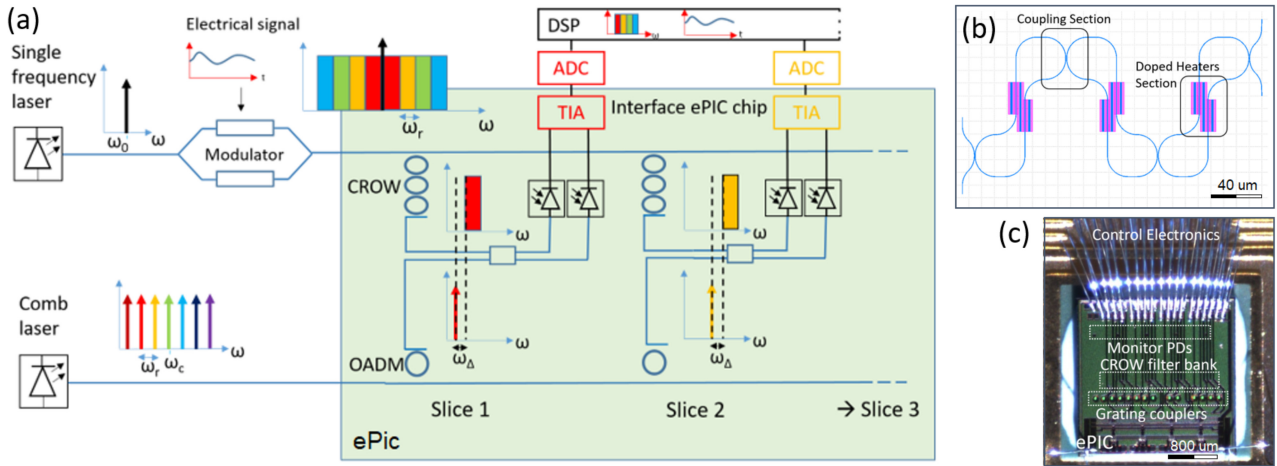
FIGURE 5. (a) Schematic of the optically enabled, spectrally-sliced ADC. Spectral slices of the modulated optical signal are combined with tones provided by an MLL and down-converted to baseband. An array of balanced on-chip photodetectors converts the spectral slices into the electrical domain using heterodyne detection. Signal reconstruction is achieved at the DSP. The green area shows the optical and electronic devices integrated in the ePIC. (b) Optimized CROW filter design. Optical coupling sections between waveguides (blue) are spatially separated from the doped heater sections (pink) to keep the coupling strengths constant. Close proximity between two phase tuners associated to the same resonator increases efficiency by leveraging thermal cross-talk. (c) Wire bonded ePIC.

to match the bandwidth of the slices. Moreover, some MLLs offer ultra-low jitter levels down into the attosecond range [15], allowing for increased ENOB at high signal frequencies [34], [35]. By applying a small offset between each LO tone and its respective slice and using heterodyne detection, we reduce the impact of flicker noise generated by the electronic amplifier stages at low offset frequencies. After converting individually each slice with reduced-bandwidth electrical ADCs featuring a high ENOB, the original RF signal can be retrieved by stitching together the signal slices in a downstream DSP. The low jitter of high-grade comb sources is also essential here, as it results in narrow RF linewidths and a high degree of correlation between the phase noise of the individual comb lines, that greatly facilitates the implementation of spectral stitching [34]–[36].

A. EPIC INTEGRATED DEVICES

Spectral slicing into four channels is implemented with as many coupled (ring-)resonator optical waveguide (CROW) filters synthetized to obtain a Chebyshev transfer function at their drop port. A third order filter was selected as a trade-off between complexity and filter roll-off steepness. The finite filter steepness also results in a spectral overlap between adjacent slices that is used by the DSP algorithm to estimate phase errors between them. Active tuning and resonant wavelength stabilization of the CROW filters is essential in this system, due to the high temperature sensitivity of silicon photonics ring resonators. The hourglass shape of the rings has been optimized to allow for efficient thermal phase tuning, while at the same time reducing thermal crosstalk between adjacent rings [37]. Therefore, we divided the rings in coupling and thermal phase tuner sections, implemented as doped resistors directly in the waveguide. As shown in Fig. 5(b), two thermal tuners nominally on opposite sides of the ring are brought close to each other by shaping the ring with an hourglass shape, to obtain the best possible

phase shifting efficiency by leveraging the thermal cross-talk between these two phase tuners, while maintaining a sufficient distance between them to prevent optical coupling. The coupling sections are separate to keep the coupling parameters constant. Moreover, sufficient separation is kept between phase shifters of different rings to reduce cross-talk and prevent thermal runaway during execution of the control algorithm. The required tuning power for the implemented CROW filters is 50 mW per FSR [37].

The same resonator shape has been adopted for the first order optical add-drop multiplexers (OADM) that select individual lines from the MLL, in which the coupling strengths have been adjusted to obtain a good tradeoff between insertion loss (IL) and crosstalk with adjacent comb lines. The dropped MLL reference tone is combined with the corresponding signal slice with 50/50 optical combiner-splitters. Multimode interferometers (MMI) offer a robust splitting ratio while featuring low IL.

Balanced integrated germanium waveguide PD pairs detect each spectral slice, feeding the generated photocurrent to a balanced TIA front-end, a variable gain amplifier (VGA) and a 50 Ω output buffer. Due to its low noise characteristic, the TIA is implemented in a differential common-emitter shunt-feedback topology [38]. An additional offset compensation network can correct possible imbalances at the input. The highest transimpedance gain is 10 kΩ, which can be reduced by the VGA to secure operation in the linear regime. The receiver shows a measured 3-dB bandwidth of 33 GHz, which also determines the maximum slice width that can be implemented. Fig. 5(c) shows a microscope image of the ePIC combining photonic and electronic devices wire bonded to a custom-designed printed circuit board (PCB).

B. EXPERIMENTAL RESULTS

In the following, the presented optical detection concept is experimentally demonstrated by spectrally sliced reception of
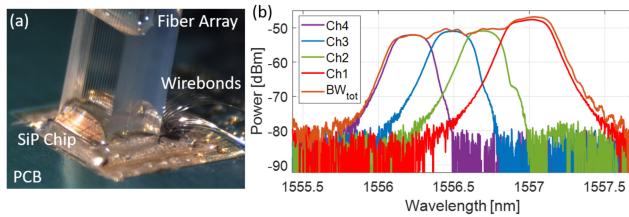
FIGURE 6. (a) Microscope image of the ePIC comprising the optical and electrical circuitry described in Section III-A. Optical signals are routed in and out of the chip by means of a permanently attached fiber array (FA). Electrical signals for the active tuning of the CROW filters are provided by a custom-designed PCB connected to the ePIC via wire bonds. (b) Spectral alignment of the CROW filters.

FIGURE 7. Constellation diagrams and corresponding constellation SNR resulting from converting a 100 GBd 16QAM signal with (a) the spectrally sliced receiver and (b) intradyne single-slice detection, for comparison.

high-speed optical data signals using the CROW filter bank from the ePIC [36]. While in this experiment, electro-optic conversion was still implemented off-chip, the demonstration may still serve to validate key aspects of the integrability of this system architecture, as the impact of the exact spectral shape of the filters onto the signal stitching and reconstruction algorithm was one of the fundamental aspects that needed to be assessed.

In our proof-of-concept experiment, optical quadrature amplitude modulated (QAM) signals are generated by a lithium-niobate IQ modulator driven by a benchtop arbitrary waveform generator and fed to the CROW-based spectral slicer following the architecture of the optically enabled ADC shown in Fig. 5. The LO tones are provided by an MZM driven by a 30 GHz sinusoidal RF signal. After the spectral slicing by the ePIC described in the previous section and shown in Fig. 6, each slice is externally mixed with a comb line by means of a directional combiner-splitter followed by a balanced photoreceiver with a 3-dB bandwidth of 43 GHz. The resulting photocurrents are digitized employing four channels of a high-speed real-time oscilloscope. Individual slices are finally stitched back together through a DSP algorithm, leading to the reconstruction of the coherent optical input signal.

For this experiment, proper tuning of the CROW filters is crucial to obtain the targeted filter shapes and spectral alignment with neighboring channels. To this end, four continuous-wave (CW) laser tones are fed through the filter bank and used as feedback signals for a tuning algorithm that maximizes the power transmitted through each filter [39] based on a round-robin-scheduling operating system. Optical taps at the CROW filter drop ports route light to on-chip monitor photodiodes that provide a feedback signal to the control algorithm. As shown in Fig. 6(b), filters are centered at the desired wavelengths and aligned relative to each other, ensuring sufficient channel spectral overlap for phase extraction and stitching, as explained in more details in [36]. An aggregate detection bandwidth of 140 GHz is achieved.

Once the desired filter alignments are obtained, the system is calibrated by measuring the complex-valued transfer function of each detection channel. To obtain these, a pilot signal, as provided by an ultra-stable mode-locked laser with a known pulse shap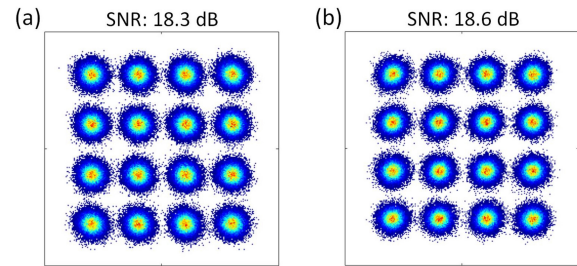e, is fed through the system, which reveals the transfer function of each channel, including CROW filters, in-line fibers, erbium doped fiber amplifier (EDFA), photodetectors and ADC transfer functions, see [36] for details.

After system calibration, the modulated optical carrier is fed to the system and the resulting sliced signals recorded. Since the detection channels still contain optical fibers and the phase offset between comb lines varies over time due to optical pulse jitter and the associated RF linewidth [40], the detected signals are impaired by time-variant phase variations. These phase variations can be compensated for by exploiting redundant information contained in the spectral overlap of neighboring slices [36]. To assess the quality of the signal detection and reconstruction, we digitize a 100 GBd 16QAM signal and compare the resulting constellation signal-to-noise ratio (SNR) to that obtained through single-slice intradyne coherent detection, see Fig. 7. We find that the penalty introduced by our system is negligible, confirming the high performance of our detection scheme. Specifically, our approach allows to significantly offload electronics and allows to scale the receiver bandwidth by increasing the number of slices or by increasing the slice bandwidth, that is still far from the capabilities of state-of-the-art on-chip germanium photodetectors in SiP ePIC technology [41].

The complete architecture shown in the green shaded area in Fig. 5 has been integrated in a single ePIC that is currently being characterized. As described above, integration of the comb source can be realized with a multi-chip assembly [30]. This also holds for the integration of the required broadband electro-optic modulators, with compact thin-film lithium niobate modulators in particular having shown both high cutoff frequencies in excess of 100 GHz and low drive voltages [42].

Further scaling of the achievable overall system bandwidth by increasing the number of slices is of course accompanied by a corresponding increase in power consumption. In order to maintain a reasonable chip complexity and power consumption, the optical signal can be split after modulation and distributed to several ePICs with filter banks tuned to different spectral regions, even though this parallel architecture would lead to a reduction in optical power budget not seen when more filters are cascaded in the same chip. Shot

noise and thermal noise, as well as amplified spontaneous emission (ASE) when optical reamplification is used, then reduce the ADC performance beyond the fundamental limits given by the MLL phase noise and pulse jitter [34], [35] and limit the scalability of the architecture when a minimum ENOB is targeted.

A substantial portion of the overall power consumption is associated to tuning the CROW filters. An average 100 mW per slice is required with the implemented thermal phase shifters to tune a 3rd order CROW filter and a single ring OADM, which is a significant overhead added to the 360 mW (4V × 90 mA) power consumption of the TIA+VGA slice in the RF electronics. The power required to tune the filters by an FSR is also relatively insensitive on the filter bandwidth and FSR [37], [43], thus forming a nearly fixed power overhead per slice. It is thus advantageous to choose relatively wide slices, with bandwidths limited by the chosen electronics technology.

IV. INTEGRATED NONLINEAR FOURIER TRANSFORM TRANSCEIVER

Ultra-wideband optically enabled ADCs have a vast range of applications, among these long-haul fiber-optic communications. Since the advent of coherent communications, the analog bandwidth, sampling rate, ENOB and dynamic range of high-speed ADCs have increasingly become drivers of the overall performance of fiber-optic links. In addition to demodulation of the complex-valued optical symbols, knowledge at the receiver of the coherent optical fields has enabled powerful link impairment mitigation techniques, covering both (linear) dispersion compensation as well as the compensation of nonlinear signal distortion. The feasibility and performance of these techniques, however, depends critically on the precision with which the optical field is digitized and thus on the performance metrics of the utilized ADCs. Consequently, optical fiber communication has been a main driver motivating advanced ADC architectures, including optically enabled ADCs. In the following, we will focus on overcoming fiber nonlinearities with help of the NFT and discuss the use of spectrally-sliced, optically enabled ADCs in this context.

Long-haul telecom network capacity is currently limited by the maximum power that can be injected into optical fibers without incurring nonlinear distortions such as self-phase modulation (SPM), cross-phase modulation (XPM) or four-wave mixing (FWM) due to the Kerr-effect [44]. Multiple techniques have been investigated to reduce the impact of these nonlinear effects, leveraging sophisticated equalization techniques such as digital back-propagation [45], nonlinear equalizers [46] and more recently neural networks [47]. The NFT constitutes a further, very powerful tool to address the Kerr effect. The NFT transforms a signal $q(t)$ into the so-called nonlinear Fourier domain, in which the normalized nonlinear Schrödinger equation reduces to a linear wave propagation problem [48]–[50]. Using the NFT, the nonlinear Kerr effect

combined with dispersion can thus simply be regarded as a linear change of the phase in the nonlinear spectrum, that can be easily adjusted using standard techniques [51].

Contrary to the linear Fourier transform, that only yields a continuous spectrum, the NFT spectrum is composed of both a continuous and a discrete spectrum. The NFT frequencies ($\lambda_c \in \mathbb{R}$, eigenvalues of the Zahkarov-Shabat scattering problem) can also be complex valued, discrete points in the complex plane ($\lambda_d \in \mathbb{C}^+, d \in \mathbb{N}$). Here, λ_c constitutes the continuous spectrum and represents the dispersive part of the signal. It is analogous to the ordinary frequency spectrum as obtained from the Fourier transform and coincides with the latter in the limit of low power. λ_d describes the discrete spectrum and corresponds to solitons in the time-domain. To transmit data, the scattering coefficient $b(\lambda)$, associated to each of the eigenvalues [48], [50], can be modulated. The inverse NFT (INFT) can then be used to create the corresponding time-domain signal. The evolution of $b(\lambda)$ through a fiber-based optical channel governed by the nonlinear Schrödinger equation can then be described by a simple, linear exponential function $b(\lambda, z) = b(\lambda, 0)e^{-2i\lambda^2 z}$, where z is the normalized distance (following the system of normalized units used in [50]). By using the NFT, higher signal powers can be used, leading to a shift of the capacity limit induced by fiber nonlinearities – the so-called nonlinear Shannon limit [44].

A major challenge of using the NFT consists in the demanding requirements for the high-speed DAC and ADC. INFT generated waveforms can have high dynamic ranges and electrical bandwidth requirements, especially if multiple discrete eigenvalues are being multiplexed into a higher order soliton. To overcome this limitation at the transmitter (Tx), we have implemented an SiP photonic integrated circuit (PIC) merging several fundamental solitons, each corresponding to a single discrete eigenvalue, in the optical domain. This way, higher-order solitons consisting of multiple eigenvalues can be created with lower requirements on the electrical hardware, thus offering a more scalable solution [52]–[54]. Similar challenges remain, however, to be addressed at the receiver (Rx). As numerically analyzed in the following, the spectral stitching technique developed for the optically enabled, spectrally sliced ADC described in Section III can be applied here to slice the optical spectrum and reduce the bandwidth requirements on the electrical ADCs and other components used in the Rx.

A block diagram of the full transmission system used to characterize the integrated Tx, together with photographs of the developed components, i.e., the PIC mounted on an RF PCB and controlled by a low-speed control board, are shown in Fig. 8. A bank of lasers is employed to provide the carriers needed to up-convert the electrical signals in the system PIC. On the electrical side, blocks of first-order solitons are modulated with the QPSK format and routed to the PIC through a custom-made multi-layer RF PCB. The system PIC contains IQ-MZMs to transduce them to the optical domain, as well as a reconfigurable optical network
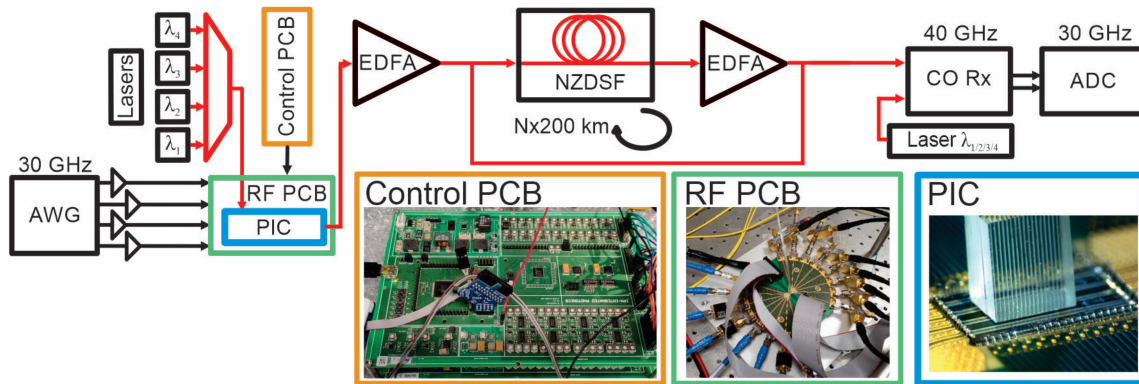
FIGURE 8. Block diagram of the investigated link, including insets with photographs of the fabricated control PCB, RF PCB and system PIC with a fiber array permanently attached for optical inputs and outputs.

merging up to four first-order solitons with different time and frequency spacings by means of programmable delay loops and multiple center-frequency-tunable CROW filters. The output signal of the PIC is amplified with an EDFA and fed into a fiber loop consisting of four spans of 50 km True-Wave non-zero-dispersion-shifted fiber (NZDSF) and four EDFAs. Finally, the signal is detected by a coherent receiver, digitized, equalized [55] and the information recovered to calculate the bit error ratio (BER). More details on the system architecture, including the PIC's block diagram, device characteristics and link budget can be found in [52]–[54], [56].

The presented system has been employed to perform experiments with 2 and 4 fundamental solitons merged at the Tx, each forming a subchannel. In these two scenarios, the center frequencies of the fundamental solitons were spaced by 30 GHz and 15 GHz and the time delays between interleaved fundamental solitons were 500 ps and 250 ps, respectively. In both cases, an entire symbol of 2 or 4 solitons fills a 1 ns launch window. The 2 and 4 subchannel experiments feature almost equal performance [54], indicating that further packing of soliton pulses in the time and frequency domains may be possible. The 4 subchannel configuration results in 8 Gbps in a 60 GHz channel. By increasing the soliton packing and exploiting both polarizations, we expect to reach a spectral efficiency of 0.5 b/s/Hz for links spanning several thousand kilometers. While this is still far below the spectral efficiency of state-of-the-art coherent transmission systems, the soliton transmission shown here can be combined with the continuous spectrum, to which the full set of techniques of coherent communications can be applied, so that the spectral efficiency described here may be considered as an addition to what is otherwise achievable.

Combination of the discrete and continuous spectra, with the latter spanning the full extent of the utilized channel width, will however require the NFT to be applied to the full channel at the Rx. This comes with its own set of challenges, as it also requires coherent digitization of the entire channel spectrum. To exemplify this problem, we compare in the following the two-subchannel link performance with two
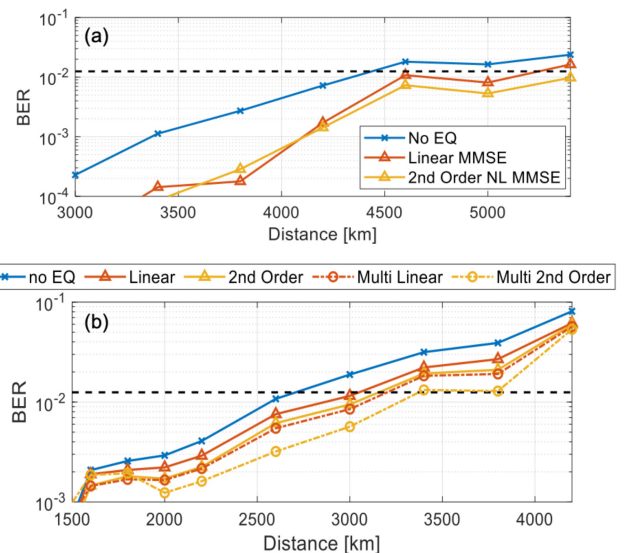

FIGURE 9. BER measurement as a function of distance with and without equalization for 2-channel transmission when (a) receiving channels individually and (b) receiving both channels together.

Rx architectures, one consisting in isolated detection of one soliton subchannel at a time, the other in the joint detection of all subchannels, which is the required method once the continuous spectrum with corresponding signals straddling all subchannels is also used.

Fig. 9(a) shows the obtained BER as a function of transmission distance when a single soliton subchannel is spectrally selected by a bandpass filter, coherently detected and independently analyzed, including single subchannel equalization techniques. The system reaches transmission distances beyond 5400 km with a BER below the assumed 14.5% overhead soft decision (SD) forward error correction (FEC) limit of 1.25×10^{-2}, once equalization employing a minimum mean square error (MMSE) algorithm has been applied.

In order to enable joint reception of the discrete and continuous spectra, receiving all soliton subchannels simultaneously by using a wideband coherent receiver represents

the most straightforward solution. To assess the feasibility of this reception scheme, an experiment in which the two subchannels are received at the same time has been performed. As apparent in Fig. 9(b), the achievable transmission distance is reduced, prior to applying equalization, from 4400 km down to 2600 km. This originates from the broader receiver filter feeding through a larger amount of amplified spontaneous emission (ASE) noise. Moreover, the increased dynamic range of the two combined fundamental soliton signals forces the power at the input of the Rx to be reduced, due to the damage threshold of the photodiodes and the finite linear range of the receiver. This is in particular true for transmission lengths resulting in soliton pulses overlapping in the time domain at the Rx, i.e., soliton collisions [57], [58]. The end result is a lower SNR after the TIA stage. As a benefit of this configuration, it becomes however also possible to apply equalization algorithms to several soliton subchannels jointly ["Multi" in Fig. 9(b)], resulting in more effective equalization.

To enable concomitant analysis of extended channel spectra, as required for exploitation of the continuous spectrum and to apply multi-soliton equalization techniques, while maintaining a high ADC resolution over reasonable analog bandwidths, an integrated Rx can be designed to implement spectral slicing and stitching, following a similar architecture to the block diagram of the optically enabled ADC shown in Fig. 5. Each spectral slice is then adapted to contain only one (or a finite number of) first-order solitons, and a portion of the continuous spectrum in case of simultaneous operation. After stitching back the slices in the digital domain [34]–[36], the full spectrum can be analyzed by the NFT.

Provided that only one first-order soliton is detected and digitized by each photoreceiver, the dynamic range and power of the optical signal for each slice remain the same as for single subchannel detection, irrespectively on the relative timing of the soliton pulses at the Rx. Beyond the obvious reduction in required sampling rate and analog bandwidth per ADC, frequency slicing can thus also improve the overall ENOB of the Rx. A few simple considerations can serve to illustrate this point. Indeed, in case of soliton collision, the full ADC range can be reduced by almost a factor four after slicing as many subchannels, corresponding in a 16x reduction of the quantization noise variance and resulting in an effective improvement of 2 bits. However, since the quantization noise of the four slices is added back together, the overall quantization noise variance only drops by 4x after stitching, resulting in a net improvement of ~1 bit. The scaling is even more favorable in case of thermal noise limited reception. In that case the total noise after stitching corresponds to that of the wideband Rx, so that close to the full 2 bit improvement can be obtained.

For demerged soliton pulses, on the other hand, the stitched reception does not improve the ADC resolution, as the ADC range can already be reduced for the wideband Rx as a consequence of the pulses being separate in time. In this
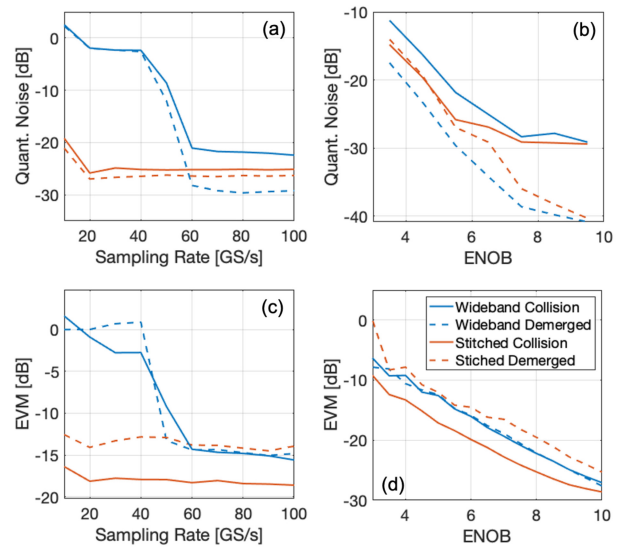

FIGURE 10. Simulated quantization noise and EVM as a function of (a),(c) sampling rate at a fixed 5.5 ENOB and (b),(d) ENOB at a fixed sampling rate (80 GS/s for wideband Rx, 20 GS/s for stitched Rx). No noise terms or equalization have been included.

scenario, the overall ENOB of the stitched receiver is actually worse by about one bit, as a consequence of the quantization noise variances of the four slices adding up. Still, the performance in terms of overall ENOB/quantization noise of the stitched receiver does not depend on whether the soliton pulses are collided or demerged, so that the performance of the stitched Rx in terms of quantization noise stays above the worst-case performance of the wideband Rx obtained with collided pulses. Moreover, slicing of the signal and the ensuing reduction of the required ADC bandwidth per slice make it easier to meet a given ENOB for the electrical ADCs, as they become less prone to aperture jitter and techniques such as oversampling followed by decimation can be used to reduce quantization noise.

However, while quantization noise extracted from numerical models is consistent with these simple considerations, the assessment of the signal quality becomes more subtle once the action of the NFT is considered.

Fig. 10 compares the simulated quantization noise and error vector magnitude (EVM) for the stitched and wideband Rx as a function of the all-electrical ADC ENOB and sampling rate for the 4 subchannel configuration (15 GHz frequency and 250 ps time spacing) assuming fixed ADC analog bandwidths of 7.5 GHz and 30 GHz, respectively (both the stitched Rx slices and the wideband Rx are modeled as using intradyne reception). No physical noise is considered in the model in order to focus on the limitations of the ADC. Multi-soliton pulses are thus obtained by applying directly the INFT to their nonlinear spectra. The length of the link is chosen such that either full soliton collision occurs, i.e., the four pulses are assumed to overlap in time, or the four solitons are fully demerged, i.e., spaced again by 250 ps but with a reverse order than in the original 1 ns launch window. The wideband Rx receives the entire

60 GHz channel bandwidth, while the stitched Rx consists of four 15 GHz slices each centered on a fundamental soliton. In panels (a) and (c), the sampling rate is varied while maintaining the electrical ADC ENOB at 5.5. In panels (b) and (d), the ENOB of the ADCs is varied while keeping the sampling rate constant (80 GS/s for the wideband Rx, 20 GS/s for each of the slices of the stitched Rx).

Results in regard to quantization noise are as expected, with the stitched Rx performing equally irrespectively of the pulse timing (for ENOBs below 6) and better (worse) than the wideband Rx in case of soliton collision (demerged pulses). It can also be observed that the quantization noise levels run into a noise floor at high ENOBs caused by the finite, 60 GHz aggregate bandwidth of both receivers, as the reconstructed signal is compared to the unfiltered one. This noise floor is higher in case of soliton collision, as a consequence of XPM leading to the center frequency of the pulses shifting outwards in the linear domain (1.5 GHz for the outer pulses), thus worsening the spectral truncation. The offset between the curves is below 1 bit due to the analyzed signals being padded by long strings of zeros, whose constant quantization error does not follow the expected probability distribution and skews the extracted average quantization noise. The trends are however as expected.

Given the 30 GHz bandwidth of the received I and Q signals, the wideband Rx requires a sampling rate of 60 GS/s in order to not feature sampling rate related EVM penalties. Below, the EVM rapidly degrades and a sampling rate of 40 GS/s is for example clearly not adequate. The stitched Rx appears more robust in that regard, since the required sampling rate is not only reduced by a factor four, at 10 GS/s the EVM is still good and only slightly above the achievable floor limited by other factors. Since this would correspond to 40 GS/s for the wideband Rx, this points towards the reception of single soliton pulses being more robust in terms of the aggregate sampling rate and is attributed to aliasing not leading to spectral reshuffling between subchannels in the stitched Rx.

The EVM dependency on ENOB, however, deviates from expectations. As expected from the previous considerations, the stitched Rx requires one bit less in the soliton collision case and, in the high ENOB regime, one more bit in the demerged case. However, the performance of the wideband Rx is not better in the demerged case as might have been expected from the reduced dynamic range. Rather, the performance of the wideband Rx is almost the same in both scenarios. As a consequence, the stitched Rx in the demerged scenario now constitutes the overall worst case. This is a consequence of the algorithms applied to perform the NFT based on the forward-backward method performing worse on demerged pulses (for both receivers), an issue that remains under investigation. However, as the number and bandwidth of subchannels increases, frequency stitching becomes a necessity in order to overcome the analog bandwidth and sampling rate limitations of state-of-the-art receivers, as the nonlinear impairment compensation

techniques used here require coherent information over the entire channel.

V. AN OUTLOOK ON OPTICALLY ENABLED ADCS IN HIGH-SPEED OPTICAL COMMUNICATIONS

After reviewing recent progress in time-interleaved and spectrally-sliced optically enabled ADCs, the question comes to mind which solution is more appropriate for future optical communication systems.

In many ways, the spectrally sliced ADC described in Section III and applied to an NFT transceiver in Section IV appears a natural choice, as it piggybacks on existing wavelength division multiplexing (WDM) infrastructure, in which phase coherence between MLL comb lines can be leveraged at the Rx to facilitate and enhance signal processing [59]. The Rx part of Fig. 5 (green shaded region) can be simply interpreted as a coherent receiver array in WDM configuration, with the additional refinement that channels spectrally overlap with each other and are later stitched together to obtain broadband coherent information. It is also scalable to high bandwidths by increasing the number of slices/WDM (sub-)channels and particularly useful in cases in which subsequent data processing leverages the availability of a broad spectrum for nonlinear impairment compensation, as in the NFT transceiver in Section IV.

We have, however, also shown that such systems inherit the jitter of both the MLL and of the electronic clock used to trigger the electrical ADCs in individual slices [34], [35]. It is only in the limit in which the spectrum is subdivided into a large number of very small slices that the overall system jitter reaches the lower limit given by the lower MLL jitter, in case of suitable ultra-low-jitter light sources [15]. However, stitching several WDM channels together after estimating phase errors by means of the overlapping spectral regions is already a hard enough problem. Further reducing the slice widths well below the capabilities of state-of-the-art coherent receivers and electrical data converters does thus not seem the best path forward. The overall aperture jitter limited ADC SNR will thus remain limited by $1/(\Delta\omega\tau_e)^2$ with $\Delta\omega$ half the slice width (the full slice width) in case of intradyne (heterodyne) reception and τ_e the jitter of the electrical clock [34], [35]. It then appears attractive to replace the electrical ADCs used in each slice by lower jitter equivalents. These can be provided by the optically triggered OE-THAs described in Section II, in particular since the required low jitter pulse train can also be provided by the MLL sourcing the reference tones for the spectral slicing. This is conceptually represented in Fig. 11.

One difficulty comes from the requirement for overlapping spectra for phase error estimation. Indeed, the FSR of the MLL, corresponding to the frequency offset between adjacent slices, then corresponds to a sampling rate that is insufficient to digitize a whole slice, even when detected in intradyne configuration. A solution may then consist in effectively increasing the repetition rate of the pulse train used to clock the OE-THAs with the method already
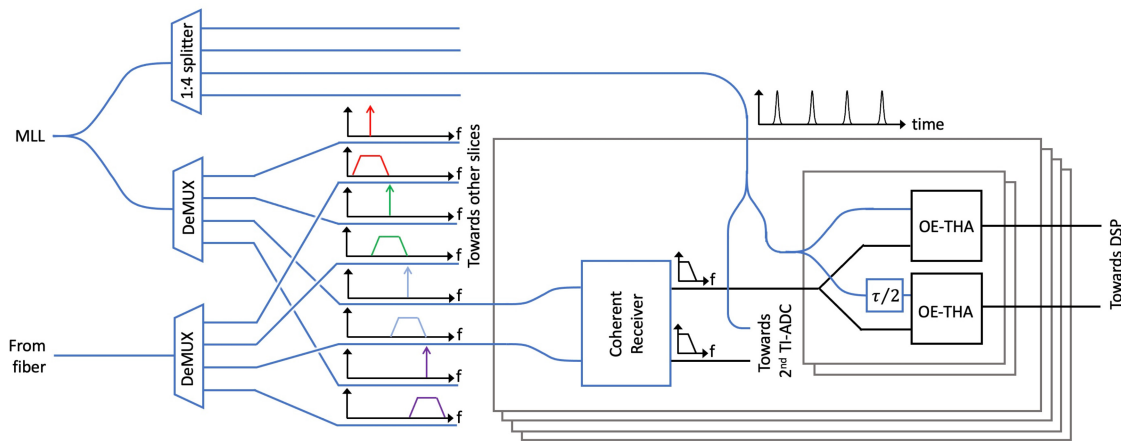
FIGURE 11. Schematic of a coherent receiver combining spectral stitching with OE-THAs and a shared MLL to obtain low-jitter and broadband reception. Four slices are exemplarily shown with spectra color-coded in red, green, blue and purple. Intradyne reception reduces the required sampling rate in each of the slices, facilitating the use of a shared MLL for both reference tone (LO) and optical clock generation. Two OE-THAs are time-interleaved in each slice and I/Q channel, in order to increase the sampling rate and effectively upconvert the optical clock.

utilized in [13] or by leveraging the time-domain Talbot effect [60].

Fig. 11 shows an alternative in which two OE-THAs are time interleaved and respectively supplied with optical pulse trains delayed by half an MLL repetition time relative to each other, so as to effectively double the optical clock relative to the comb FSR. The resulting Nyquist frequency of one FSR is then sufficient to allow ample spectral overlap between the slices and spectral stitching, if these are detected by means of intradyne detection (halving the required electrical spectra). Since the current OE-THAs need to be interleaved in any case in order to exploit their whole analog bandwidth, as described in Section II, this appears a natural solution.

VI. CONCLUSION

In summary, we have shown two integrated, optically enabled ADC architectures based on time-interleaved, optically triggered track-and-hold amplifiers, as well as spectral slicing of an optical signal, with respective frequency conversion shown up to 65 GHz and 140 GHz, respectively. The spectral slicing method in particular is readily adaptable to higher frequencies by increasing the number of slices or their bandwidth. Even then, low jitter ADCs remain essential for use in each of the slices, as their jitter translates to the overall system jitter. Since the spectrally-sliced and time-interleaved architectures shown here can share a common mode-locked laser, they may be ideally suited to be operated together in order to reach the upper effective number of bits limit as afforded by ultra-low-jitter pulsed laser sources. The low power consumption of the presented OE-THA circuit plays an important role in enabling scalability.

The mitigation of nonlinear impairments in general, and the use of the nonlinear Fourier transform in particular, provide examples in which the use of such ultra-broadband data converters is a key enabler, since the incoming optical spectrum can no longer be considered a juxtaposition of otherwise non-interacting optical channels. These rather need to be coherently analyzed together.

REFERENCES

[1] J. Singh, S. Ponnuru, and U. Madhow, "Multi-gigabit communication: The ADC bottleneck[1]," in *Proc. IEEE Int. Conf. Ultra-Wideband (ICUWB)*, Vancouver, BC, Canada, Sep. 2009, pp. 22–27.

[2] M. J. Wale, "Advanced modulation formats in data centre communications," in *Proc. 2nd Symp. Opt. Interconnects Data Centres Europ. Conf. Integr. Opt. (ECOC)*, Cannes, France, Sep. 2014, pp. 1–13.

[3] N. Eiselt *et al.*, "Performance comparison of 112-Gb/s DMT, Nyquist PAM4, and partial-response PAM4 for future 5G Ethernet-based fronthaul architecture," *J. Lightw. Technol.*, vol. 36, no. 10, pp. 1807–1814, May 15, 2018.

[4] C. Laperle and M. O'Sullivan, "Advances in high-speed DACs, ADCs, and DSP for optical coherent transceivers," *J. Lightw. Technol.*, vol. 32, no. 4, pp. 629–643, Feb. 15, 2014.

[5] B. Razavi, "Design considerations for interleaved ADCs," *IEEE J. Solid-State Circuits*, vol. 48, no. 8, pp. 1806–1817, Aug. 2013.

[6] A. Buchwald, "High-speed time interleaved ADCs," *IEEE Commun. Mag.*, vol. 54, no. 4, pp. 71–77, Apr. 2016.

[7] G. Ding, C. Dehollain, M. Declercq, and K. Azadet, "Frequency-interleaving technique for high-speed A/D conversion," in *Proc. Int. Symp. Circuits Syst. (ISCAS)*, Bangkok, Thailand, 2003, pp. 857–860.

[8] P. J. Pupalaikis *et al.*, "Technologies for very high bandwidth real-time oscilloscopes," in *Proc. IEEE Bipolar/BiCMOS Circuits Technol. Meeting (BCTM)*, Coronado, CA, USA, 2014, pp. 128–135.

[9] L. Passetti, A. C. Galetto, D. J. Hernando, D. Morero, B. T. Reyes, and M. R. Hueda, "Backpropagation-based background compensation of frequency interleaved ADC for coherent optical receivers," in *Proc. IEEE Int. Symp. Circuits Syst. (ISCAS)*, Seville, Spain, 2020, pp. 1–5.

[10] A. V. Krishnamoorthy *et al.*, "Progress in low-power switched optical interconnects," *IEEE J. Sel. Topics Quantum Electron.*, vol. 17, no. 2, pp. 357–376, Mar./Apr. 2011.

[11] D. Marpaung, J. Yao, and J. Capmany, "Integrated microwave photonics," *Nat. Photon.*, vol. 13, pp. 80–90, Feb. 2019.

[12] G. C. Valley, "Photonic analog-to-digital converters," *Opt. Expr.*, vol. 15, no. 5, pp. 1955–1982, 2007.

[13] A. Khilo *et al.*, "Photonic ADC: Overcoming the bottleneck of electronic jitter," *Opt. Expr.*, vol. 20, no. 4, pp. 4454–4469, 2012.

[14] G. Gao and L. Lei, "Photonics-based broadband RF spectrum measurement with sliced coherent detection and spectrum stitching technique," *IEEE Photon. J.*, vol. 9, no. 5, Oct. 2017, Art. no. 5503111.

[15] A. J. Benedick, J. G. Fujimoto, and F. X. Kärtner, "Optical flywheels with attosecond jitter," *Nat. Photon.*, vol. 6, no. 2, pp. 97–100, 2012.

[16] G. Masini, G. Capellini, J. Witzens, and C. Gunn, "High-speed, monolithic CMOS receivers at 1550nm with Ge on Si waveguide photodetectors," in *Proc. IEEE Lasers Electro-Opt. Soc. Annu. Meeting Conf. (LEOS)*, Lake Buena Vista, FL, USA, 2007, pp. 848–849.

[17] S. Ummenthala et al., "Hybrid electro-optic modulator combining silicon photonic slot waveguides with high-k radio-frequency slotlines," *Optica*, vol. 8, no. 4, pp. 511–519, 2021.

[18] S. Ummenthala et al., "THz-to-optical conversion in wireless communications using an ultra-broadband plasmonic modulator," *Nat. Photon.*, vol. 13, no. 8, pp. 519–524, 2019.

[19] B. Krueger et al., "A monolithically integrated, optically clocked 10 GS/s sampler with a bandwidth of >30 GHz and a jitter of <30 fs in photonic SiGe BiCMOS technology," in *Proc. IEEE Custom Integr. Circuits Conf. (CICC)*, Austin, TX, USA, 2017, pp. 1–4.

[20] M. Weizel, J. C. Scheytt, F. X. Kärtner, and J. Witzens, "Optically clocked switched-emitter-follower THA in a photonic SiGe BiCMOS technology," *Opt. Expr.*, vol. 29, no. 11, pp. 16312–16322, 2021.

[21] L. Deniel et al., "Silicon photonics phase and intensity modulators for flat frequency combs generation," *Opt. Expr.*, to be published.

[22] D. Knoll et al., "High-performance photonic BiCMOS process for the fabrication of high-bandwidth electronic-photonic integrated circuits," in *Proc. IEEE Int. Electron Devices Meeting (IEDM)*, Washington, DC, USA, Dec. 2015, pp. 1–4.

[23] S. Gudyriev, J. C. Scheytt, L. Yan, C. Meuer, and L. Zimmermann, "Fully-differential, DC-coupled, Self-biased, monolithically-integrated optical receiver in 0.25 μm photonic BiCMOS technology for multichannel fiber links," in *Proc. IEEE Bipolar/BiCMOS Circuits Technol. Meeting (BCTM)*, Miami, FL, USA, 2017, pp. 110–113.

[24] K. Li et al., "Co-design of a differential transimpedance amplifier and balanced photodetector for a sub-pJ/bit silicon photonics receiver," *Opt. Expr.*, vol. 28, no. 9, pp. 14038–14054, 2020.

[25] E. Krune, K. Jamshidi, K. Voigt, L. Zimmermann, and K. Petermann, "Jitter analysis of optical clock distribution networks in silicon photonics," *IEEE J. Lightw. Technol.*, vol. 32, no. 22, pp. 4378–4385, Nov. 15, 2014.

[26] N. Singh, E. Ippen, and F. X. Kärtner, "Towards CW modelocked laser on chip—A large mode area and NLI for stretched pulse mode locking," *Opt. Expr.*, vol. 28, no. 15, pp. 22562–22579, 2020.

[27] T. J. Kippenberg, A. L. Gaeta, M. Lipson, and M. L. Gorodetsky, "Dissipative Kerr solitons in optical microresonators," *Science*, vol. 361, no. 6402, 2018, Art. no. aan8083.

[28] W. Weng et al., "Gain-switched semiconductor laser driven soliton microcombs," *Nat. Commun.*, vol. 12, p. 1425, Mar. 2021.

[29] B. Stern, X. Ji, Y. Okawachi, A. L. Gaeta, and M. Lipson, "Battery-operated integrated frequency comb generator," *Nature*, vol. 562, pp. 401–405, Oct. 2018.

[30] M. Blaicher et al., "Hybrid multi-chip assembly of optical communication engines by in situ 3D nano-lithography," *Light Sci. Appl.*, vol. 9, p. 71, Apr. 2020.

[31] B. Murmann. (2021). *ADC Performance Survey 1997–2021*. [Online]. Available: http://web.stanford.edu/~murmann/adcsurvey.html

[32] J. Witzens, "High-speed silicon photonics modulators," *Proc. IEEE*, vol. 106, no. 12, pp. 2158–2182, Dec. 2018.

[33] M. Weizel, F. X. Kaertner, J. Witzens and J. C. Scheytt, "Photonic analog-to-digital-converters—Comparison of a MZM-sampler with an optoelectronic switched-emitter-follower sampler," in *Proc. 21st ITG Symp. Photon. Netw.*, 2020, pp. 119–124.

[34] A. Zazzi et al., "Fundamental limitations of spectrally-sliced optically enabled data converters arising from MLL timing jitter," *Opt. Expr.*, vol. 28, no. 13, pp. 18790–18813, 2020.

[35] A. Zazzi et al., "Mode-locked timing jitter limitation in optically enabled, spectrally sliced ADCs," in *Proc. 21st ITG Symp. Photon. Netw.*, 2020, pp. 114–118.

[36] D. Fang et al., "Optical arbitrary waveform measurement (OAWM) on the silicon photonic platform," in *Proc. Opt. Fiber Netw. Commun. Conf. Exhibit.(OFC)*, San Francisco, CA, USA, Jun. 2021, pp. 1–3.

[37] J. Müller et al. (Sep. 2021). *Optimized Hourglass-Shaped Resonators for Efficient Thermal Tuning of CROW Filters With Reduced Crosstalk*. [Online]. Available: https://doi.org/10.31224/osf.io/vr94e

[38] S. Gudyriev et al., "Coherent ePIC receiver for 64 GBaud QPSK in 0.25 μm photonic BiCMOS technology," *J. Lightw. Technol.*, vol. 37, no. 1, pp. 103–109, Jan. 1, 2019.

[39] J. C. C. Mak, W. D. Sacher, T. Xue, J. C. Mikkelsen, Z. Yong, and J. K. S. Poon, "Automatic resonance alignment of high-order microring filters," *IEEE J. Quantum Electron.*, vol. 15, no. 11, Nov. 2015, Art. no. 0600411.

[40] R. Rosales, K. Merghem, A. Martinez, F. Lelarge, A. Accard, and A. Ramdane, "Timing jitter from the optical spectrum in semiconductor passively mode locked lasers," *Opt. Expr.*, vol. 20, no. 8, pp. 9151–9160, 2012.

[41] S. Lischke et al., "High bandwidth, high responsivity waveguide-coupled germanium p-i-n photodiode," *Opt. Expr.*, vol. 23, no. 21, pp. 27213–27220, Oct. 2015.

[42] C. Wang et al., "Integrated lithium niobate electro-optic modulators operating at CMOS-compatible voltages," *Nature*, vol. 562, pp. 101–104, Sep. 2018.

[43] J. Müller et al., "Silicon photonics WDM transmitter with single section semiconductor mode-locked laser," *Adv. Opt. Technol.*, vol. 4, no. 2, pp. 119–145, 2015.

[44] R.-J. Essiambre, G. Kramer, P. J. Winzer, G. J. Foschini, and B. Goebel, "Capacity limits of optical fiber networks," *IEEE J. Lightw. Technol.*, vol. 28, no. 4, pp. 662–701, Feb. 15, 2010.

[45] E. Ip and J. M. Kahn, "Compensation of dispersion and nonlinear impairments using digital backpropagation," *IEEE J. Lightw. Technol.*, vol. 26, no. 20, pp. 3416–3425, Oct. 15, 2008.

[46] Y. Gao, F. Zhang, L. Dou, Z. Chen, and A. Xu, "Intra-channel nonlinearities mitigation in pseudo-linear coherent QPSK transmission systems via nonlinear electrical equalizer," *Opt. Commun.*, vol. 282, no. 12, pp. 221–425, 2009.

[47] E. Giacoumidis et al., "Intra and inter-channel nonlinearity compensation in WDM coherent optical OFDM using artificial neural network based nonlinear equalization," in *Proc. Opt. Fiber Netw. Commun. Conf. (OFC)*, Los Angeles, CA, USA, 2017, pp. 1–3.

[48] M. I. Yousefi and F. R. Kschischang, "Information transmission using the nonlinear Fourier transform, part I: Mathematical tools," *IEEE Trans. Inf. Theory*, vol. 60, no. 7, pp. 4312–4328, Jul. 2014.

[49] S. T. Le, V. Aref, and H. Buelow, "Nonlinear signal multiplexing for communication beyond the kerr nonlinearity limit," *Nat. Photon.*, vol. 11, no. 9, pp. 570–576, 2017.

[50] S. K. Turitsyn et al., "Nonlinear Fourier transform for optical data processing and transmission: Advances and perspectives," *Optica*, vol. 4, no. 3, pp. 307–322, 2017.

[51] S. Li, J. Koch, and S. Pachnicke, "Optical signal processing in the discrete nonlinear frequency domain," in *Proc. Opt. Fiber Netw. Commun. Conf. Exhibit. (OFC)*, San Diego, CA, USA, Mar. 2018, pp. 1–3.

[52] A. Moscoso-Mártir et al., "Silicon photonics DWDM NLFT soliton transmitter implementation and link budget assessment," in *Proc. Eur. Conf. Integr. Opt. (ECIO)*, Jun. 2020, Art. no. 12.A. [Online]. Available: arxiv.org/abs/2003.08358

[53] J. Koch et al., "Experimental demonstration of a silicon-photonics WDM NFT soliton transmitter," in *Proc. Opt. Fiber Netw. Commun. Conf. (OFC)*, San Francisco, CA, USA, Jun. 2021, pp. 1–3.

[54] A. Moscoso-Mártir et al., "Silicon photonics integrated circuits for nonlinear Fourier transform based transmission," in *Proc. 47th Eur. Conf. Opt. Commun. (ECOC)*, Sep. 2021, Art. no. We4G.5.

[55] J. Koch, K. Chan, C. G. Schaeffer, and S. Pachnicke, "Signal processing techniques for optical transmission based on Eigenvalue communication," *IEEE J. Sel. Topics Quantum Electron.*, vol. 27, no. 3, May-Jun. 2021, Art. no. 5100214.

[56] F. Merget et al., "Silicon photonics plasma-modulators with advanced transmission line design," *Opt. Expr.*, vol. 21, no. 17, pp. 19593–19607, Aug. 2013.

[57] J. Koch, S. Li, and S. Pachnicke, "Transmission of higher order solitons created by optical multiplexing," *IEEE J. Lightw. Technol.*, vol. 37, no. 3, pp. 933–941, Feb. 1, 2019.

[58] J. Koch, A. Moscoso-Martir, J. Mueller, F. Merget, S. Pachnicke, and J. Witzens, "Silicon photonics DWDM NLFT soliton transmitter," in *Proc. 21st ITG Symp. Photon. Netw. (VDE)*, 2020, pp. 93–100.

[59] J. Witzens, "WDM telecommunications link with coherent detection and optical frequency comb sources," U.S. Patent US9 088 371 B2, Apr. 2012.

[60] N. Neumann, M. Haas, D. Plettemeier, T. Dresden, and C. Schaeffer, "Talbot effect supported millimeter wave generation," in *Proc. 18th Inf. Conf. Microw. Radar Wireless Commun.*, Vilnius, Lithuania, Jun. 2010, pp. 1–3.